Static and Dynamic Aspects of Black Silicon Formation

David Abi Saab and Philippe Basset
Université Paris-Est, ESYCOM, ESIEE Paris, 93162 Noisy le Grand, France

Matthew J. Pierotti and Matthew L. Trawick
University of Richmond, Richmond, 23173 Virginia, USA

Dan E. Angelescu
Université Paris-Est, ESYCOM, ESIEE Paris, 93162 Noisy le Grand, France
(Received 22 September 2014; published 31 December 2014)

We present a combination of experimental data and modeling that explains some of the important characteristics of black silicon (BSi) developed in cryogenic reactive ion etching (RIE) processes, including static properties (dependence of resulting topography on process parameters) and dynamic aspects (evolution of topography with process time). We generate a phase diagram predicting the RIE parameter combinations giving rise to different BSi geometries and show that the topographic details of BSi explain the metamaterial characteristics that are responsible for its low reflectivity. In particular, the unique combination of needle and hole features of various heights and depths, which is captured by our model and confirmed by focused ion beam nanotomography, creates a uniquely smooth transition in refractive index. The model also correctly describes dynamical characteristics, such as the dependence of aspect ratio on process time, and the prediction of new etching fronts appearing at topographical saddle points during the incipient stages of BSi development—a phenomenon reported here for the first time.

DOI: 10.1103/PhysRevLett.113.265502 PACS numbers: 81.65.Cf, 05.40.-a, 68.55.-a

Significant research interest has been dedicated recently to methods capable of creating high aspect-ratio (HAR) nanoscale patterns in silicon. Maskless techniques, resulting in self-generated patterns over large substrate areas, are of particular interest due to their inherent simplicity and low process cost. Black silicon (BSi), a generic name for light-absorbing, densely packed patterns of subwavelength columnar silicon structures obtained by a number of techniques such as cryogenic reactive ion etching (RIE) [1] or laser ablation [2], is one example of such material. BSi has been used in a wide range of applications, ranging from high-efficiency absorbers for solar cells [3–6], to infrared-optimized photodetectors [7], and to superhydrophobic surfaces [8] that can find applications in microelectromechanical devices such as sensors [9].

BSi produced by cryogenic RIE involves the use of an inductively coupled plasma (ICP) RIE chamber, where the generation of ions and their acceleration towards the sample are controlled independently by the ICP radio-frequency power and the voltage bias. The usual gas compounds consist of SF_6 that chemically etches the silicon and O_2 that is involved in the formation of a conformal passivation layer (with enhanced strengths at temperatures less than −80 °C); in addition, a directional etching of the passivation layer produced by SF_x^+ ions is controlled with the adjustable voltage bias. The molecular interactions during BSi formation in SF_6/O_2 based plasmas in cryogenic RIE have been previously described [10]: The etching plasma SF_6 produces SF_x^+ ions and F^* radicals. The radicals diffuse toward the substrate and produce an isotropic chemical etching reaction with silicon. Simultaneously, the O^* radicals produced in the oxygen plasma also diffuse toward the substrate creating a $Si_xO_yF_z$ passivation layer that protects the silicon from chemical etching. While this layer cannot be removed by the F^* radicals, it is susceptible to physical directional etching by the SF_x^+ ions. Because of the ions' trajectory, the etching is stronger on horizontal surfaces than on vertical walls. When the passivation layer formation and etching rates are similar (controlled by the SF_6/O_2 gas flow ratio), the competition between the two processes leads to anisotropic etching and the formation of HAR structures.

The mechanism by which a complex topography such as BSi (which can range from arrays of needles [1] to networks of connected holes [10], with various aspect ratios and length scales [11]) can be generated from a nearly atomically flat surface by a uniform RIE etching process is not well understood. In our experience, crystalline orientation (including polycrystallinity), doping type and level, and surface roughness have little effect on the BSi formation process. Multiple hypotheses have been proposed regarding the formation mechanisms for BSi topography, such as micromasking effects due to growth or redeposition onto the substrate, or due to variations in the initial oxide layer [1,12]. Self-shadowing has long been proposed as an interface-roughening mechanism [13], and interface growth models have been developed that incorporate such long-range effects as the dependence of growth rate on local exposure angle [14]. Monte Carlo–based

 © 2014 American Physical Society

simulations of initial roughening due to self-shadowing have also been performed by a number of groups for both RIE and chemical vapor or sputtering depositions [15,16], but these focus primarily on the onset of roughening and do not provide insight for HARs (> 3) such as those observed in BSi [10,11]. Such HARs impose significant difficulties even for accurately imaging BSi. A number of techniques have been applied to BSi characterization, such as scanning electron microscopy (SEM) in top view, side view, and cross section [10,11], sometimes combined with destructive focused ion beam (FIB) nanotomography, consisting of a dual beam configuration of a fine beam of Gallium ions that allow precise incremental etching steps of the BSi structures combined with SEM micrograph acquisitions, to obtain accurate 3D structure details [12]. Nondestructive SEM gray scale analysis has recently been attempted [17] for obtaining full topography information from a top-view SEM image; however, such techniques are limited by the detector's dynamic range, especially when analyzing HAR structures typical of fully developed BSi.

In this report we provide experimental data and a consistent model that is capable of explaining both the initial formation of BSi nanostructures from a polished silicon substrate and their subsequent late-time evolution. The model is controlled by parameters such as silicon etch rate, passivation growth rate, and passivation etch rate, which are directly related to plasma RIE control parameters (SF_6 and O_2 content, process temperature, and voltage bias). An important feature of the model is the inclusion, in a manner similar to [14], of a geometric occlusion factor that is responsible for the hindered access of process gases at the base of HAR structures or holes. We compare the predictions of the model with observation of physical BSi samples obtained at different stages of cryogenic RIE processes utilizing different process parameters, such as varying ratios of O_2 and SF_6 gases and different plasma bias voltages [11]. Sample visualization is performed by combining several state-of-the-art imaging and 3D reconstruction techniques: time lapse etching combined with SEM gray scale analysis; FIB nanotomography; cross-sectional and side-view SEM imaging. We are able to reproduce, through this relatively simple model, the dependence of the static BSi geometrical parameters (feature size, aspect ratio, and height distribution) on RIE plasma parameters. A phase diagram that is consistent with experimental data is generated, with clearly identified regions of no etching, BSi formation, and uniform etching. The exceptional low reflectivity characteristics of BSi are explained by its specific geometry consisting of needles and holes of various heights and depths which give it exceptional metacharacteristics, displaying (in both experimental data and simulation) a very smooth variation of silicon content (and hence of refractive index) from the top to the bottom of the structures. The model predicts the same variation of aspect ratio (calculated as the height of structures divided by average structure separation) with time as observed in experiments; moreover, the dynamics of BSi formation provided by our model shows both qualitative and quantitative agreement with time-lapse experiments, including the prediction of new etch fronts that appear at topographical saddle points (a phenomenon never reported before).

The model data are stored in two bidimensional arrays (Z_{SI} and Z_{PL}) corresponding to the silicon substrate height (with initial values imposed by the chosen substrate geometry), and, respectively, the passivation layer thickness as measured normal to the substrate (with null initial value). Different initial substrate geometries have been used: that of a polished silicon wafer with residual roughness characterized by independent atomic force microscopy studies [15], and that of BSi obtained at different stages of time-lapse etching or SEM gray scale imaging experiments. The simulation implements the three main processes that occur in cryogenic RIE: passivation layer formation, passivation layer etching, and silicon etching, which are repeated in discretized time increments until the final process time is reached. Because the passivation layer formation and silicon etching processes depend on free diffusion of radicals to the substrate (O_2 and SF_6, respectively) [10], they are more efficient in areas readily exposed to the plasma (e.g., top of features) than in areas occluded by surrounding structures (e.g., bottom of trenches and holes). It is important to note that at low pressures (less than 10 Pa) that are typical in cryogenic RIE processes, the mean free path of radicals is significantly longer than the scale of BSi structures. Passivation layer formation and silicon etching rates therefore depend on the geometric occlusion level and can be considered proportional to the local solid angle Ω of unobstructed exposure to the plasma. By contrast, passivation layer etching relies primarily on ions being accelerated towards the sample by the plasma dc voltage bias, which physically removes the passivation layer. Such ions impact the wafer with high energies on close-to-vertical trajectories, leading to etching rates that depend on the plasma dc bias setting but not on geometric occlusion. Since passivation layer formation is a conformal process whereas its etching is highly directional, the effective passivation thickness that is presented to the etching ions depends on local surface normal angle, the passivation layer etching rate on horizontal surfaces being higher than on close-to-vertical walls. The main model parameters are close analogs to those controlling cryogenic RIE processes: maximum passivation formation rate v_{pf} (related to the O_2 concentration and temperature), maximum passivation etching rate v_{pe} (related to bias voltage), maximum silicon etching rate v_{se} (related to SF_6 concentration), and total process time t_{proc}; all parameters are also affected by plasma power. Secondary collisions are ignored; ion-substrate interactions are assumed to have a sticking coefficient of 1. Because the height function Z_{SI} is single valued, overhanging features (which we never observe experimentally) cannot be modeled using the current approach.

At each time step the algorithm computes the angle α_n between surface normal and the vertical direction, as well as the plasma exposure solid angle Ω everywhere on the surface, using a computational approach similar to [14].

Simulation continues by modeling passivation layer growth and etching. The model implements self-limiting growth that is linear at early stages but progressively slows down as the passivation layer thickens. Such behavior is introduced through the use of a sigmoid function f to map what would be the thickness of the passivation layer $Z_{\mathrm{PL}}^{\mathrm{lin}}$, assuming unhindered linear growth, to a range of actual thickness $Z_{\mathrm{PL}} = f(Z_{\mathrm{PL}}^{\mathrm{lin}})$ that is bounded by a maximum passivation layer thickness $Z_{\mathrm{PL}}^{\mathrm{max}}$:

$$Z_{\mathrm{PL}} = f(Z_{\mathrm{PL}}^{\mathrm{lin}}) = Z_{\mathrm{PL}}^{\mathrm{max}}\left[\frac{2}{1+\exp(\frac{-2Z_{\mathrm{PL}}^{\mathrm{lin}}}{Z_{\mathrm{PL}}^{\mathrm{max}}})} - 1\right]. \quad (1)$$

The passivation layer thickness at the end of the current time step is then provided by

$$Z_{\mathrm{PL}}(t+dt) = f\left(f^{-1}(Z_{\mathrm{PL}}(t)) + \frac{v_{\mathrm{pf}}\Omega dt}{4\pi}\right) - \cos(\alpha_n)v_{\mathrm{pe}}dt, \quad (2)$$

which includes the directional etching term that is dependent on normal angle α_n. Since the passivation layer etching cannot be larger than the thickness of the passivation layer itself, Z_{PL} obtained from Eq. (2) is truncated at 0 wherever it reaches negative values, which corresponds to bare silicon being reached after a time interval $\delta t < dt$, with

$$\delta t = \frac{f(f^{-1}(Z_{\mathrm{PL}}(t)) + \frac{v_{\mathrm{pf}}\Omega dt}{4\pi})}{\cos(\alpha_n)v_{\mathrm{pe}}}. \quad (3)$$

Silicon etching will only be performed in areas where no passivation layer is present, for the time interval $dt - \delta t$ that is remaining in the current simulation step. The silicon height at the end of the silicon etching step is, therefore,

$$Z_{\mathrm{SI}}(t+dt) = \begin{cases} Z_{\mathrm{SI}}(t) - \frac{v_{\mathrm{se}}\Omega(dt-\delta t)}{\cos(\alpha_n)4\pi} & \text{if } Z_{\mathrm{PL}}(t+dt) = 0 \\ Z_{\mathrm{SI}}(t) & \text{otherwise.} \end{cases} \quad (4)$$

We note that in Eq. (4) the amount of silicon etched is affected by occlusion through the local plasma exposure angle Ω, whereas the isotropic nature of the etching is accounted for by the inverse dependence on $\cos(\alpha_n)$. The silicon height is additionally reduced at each step by the amount of new passivation layer formation to account for silicon consumed in the passivation reaction. (Additional information on the modeling available as Supplemental Material [18].)

By varying v_{pe} and v_{pf} at fixed v_{se} and t_{proc}, we simulated the growth of BSi structures from planar surfaces in different plasma conditions (variation of v_{pf} is analogous to a change in the SF_6/O_2 gas ratio in the plasma). The results are summarized in the phase diagram at the top of Fig. 1, where the area with high standard deviation of height shows a delimited phase-space area where BSi is formed. Consistent with experimental observations, at low v_{pe} and high v_{pf}, no etching is performed (the surface is overpassivated), whereas at high v_{pe} and low v_{pf}, the etching is uniform with no features present (not enough passivation). The model predicts that the BSi phase disappears for combinations of large v_{pe} and v_{pf}, suggesting that a gradual transition from no-etch to uniform etch behavior is possible without the intermediate BSi phase.

The bottom of Fig. 1 shows the strong similarity between simulation results at various v_{pf} values and SEM images from a previous parametric study, where the effect of SF_6/O_2 on the geometry of the resulting BSi structures was measured [11]. We notice that the BSi obtained in a low oxygen content process (low v_{pf}) consists of sharp HAR features (the surface in this case appears black, with visible light reflectivity below 1% [11]), which become progressively shallower and rounder as the oxygen content (or, analogously, v_{pf}) is increased (in which case the surface appears grayer). This behavior is the basis for the empirical "black silicon method," which has become the standard method used to optimize cryogenic plasma conditions when perfectly vertical etch profiles are required [1].

BSi is an example of metamaterial: its low reflectivity at wavelengths larger than feature size can be explained by the smooth refractive index change between silicon and air, which inhibits reflection of incident light. The more gradual this transition, the lower the reflectivity, hence the interest of HAR structures. To measure the silicon content vs depth for

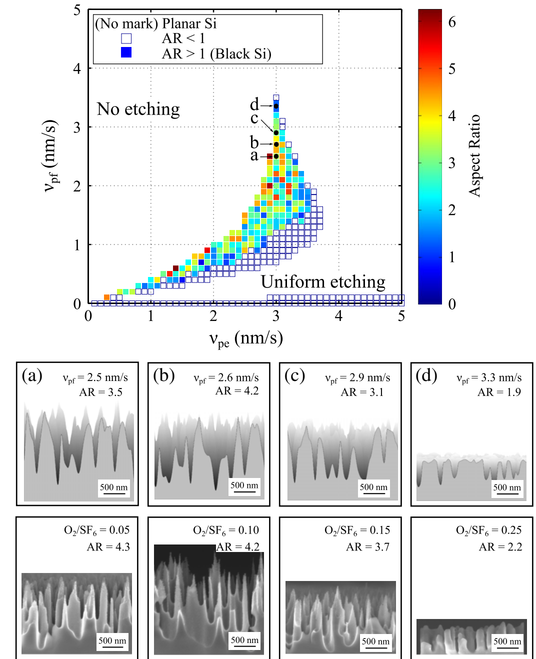

FIG. 1 (color online). Top: phase diagram of etch behavior dependence on v_{pe} and v_{pf}, the other parameters being fixed ($v_{\mathrm{se}} = 30$ nm/s and $t_{\mathrm{proc}} = 10$ min). The region with aspect ratio (AR) greater than one was interpreted as the characteristic feature of BSi presence. Bottom: cross-sectional views of resulting geometries simulation for the BSi formation conditions identified as a, b, c, d in the phase diagram at the top compared with experimental data (reproduced from [11]).

actual BSi samples, we used an original destructive FIB nanotomography technique consisting of successive FIB slicing starting from the top of the structures, and subsequent SEM imaging of each slice. The silicon content corresponding to each slice could thus be determined, and a complete three-dimensional model of the BSi sample built. Figure 2 shows the excellent agreement that is obtained between simulation and measurement, and proves that the BSi geometry provides, indeed, a very smooth transition from silicon to air. The smoothness is a direct consequence of the characteristic features of BSi, which consist of a combination of sharp "needles" at the top and rounded "holes" at the bottom, extending to various heights and depths (as seen in the insets to Fig. 2). It is interesting to note that such a smooth transition cannot be obtained with standard lithographic texturing especially at subwavelength scales. Simulations of the mean specular reflectance on multiple dielectric layers, using the silicon-air ratio obtained by FIB nanotomography, provide results consistent with actual reflectance measurements of the same sample (0.42% and 0.43% for simulated and measured mean specular reflectance, respectively, with wavelength range between 400 and 1000 nm).

To gain insight into the formation mechanisms of BSi, we performed two dynamic studies. We first simulated the evolution of the BSi geometry over time, starting with a substrate that is flat but with random pixelwise roughness of 0.5 nm (animation available as Supplemental Material [18]). The simulation data were found to be in good agreement with actual measurements performed on distinct samples subjected to cryogenic RIE for different amounts of time, and imaged with top-view, tilt-view, and cross-sectional SEM [11]. In particular, what is observed in both experiment and simulation is that BSi appears after a few minutes of process time, its aspect ratio increasing rapidly over the next few minutes before finally leveling off (Fig. 3). The simulations reveal the detailed structure of BSi at different stages of its evolution: at $t_{proc} = 7$ min, the initial roughness length scale is amplified by a factor of approximately 20, generating a network of holes at the planar surface, which then grow and densify as they are etched progressively deeper into the substrate (insets to Fig. 3). At some point, as the etching progresses, all the flat portions of the substrate are etched away, leaving behind the network of needles characteristic of BSi, consistent with experimental observations [11,12]. At the same time, the initial holes continue to be etched deeper into the substrate, causing the geometry observed at the bottom of the BSi structures (and illustrated in the insets to Fig. 2). Increase in the aspect ratio then slows down as the geometry evolves towards a configuration that balances the etch rates of needles and holes. As Fig. 1 confirms, the ultimate aspect ratio that can be obtained is process dependent.

We also performed a series of time-lapse experiments in which we etched an initially planar substrate in multiple single-minute intervals, imaging the same sample region with nondestructive top-view and tilt-view SEM after each etching step. We have employed lithographically defined fiducial marks in order to identify the area of investigation under the SEM after the different time-lapse RIE etching steps. This procedure allowed us to observe, dynamically, how the etching proceeds on a sample that has already developed incipient BSi [Fig. 4(a)]. We noticed an interesting phenomenon: new holes tend to be etched preferentially at topographical saddle points [Fig. 4(c)]. The observed phenomenology can be explained by the fact that the initial flat surface of the Si sample is unstable to hole formation under RIE since the etching of the passivation layer is anisotropic (ion bombardment), and thus unaffected by hole formation, whereas the passivation layer formation is hindered by diffusion at the bottoms of the holes. The bottoms of the holes therefore see reduced passivation, and hence the

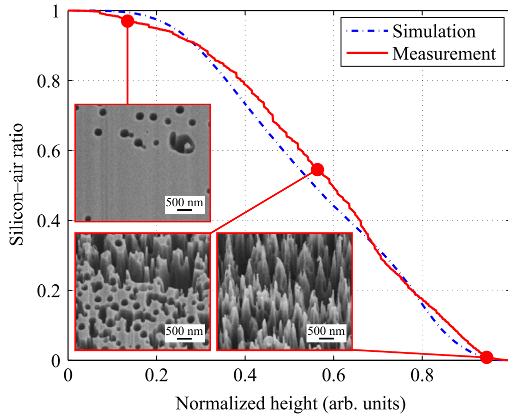

FIG. 2 (color online). Silicon content vs depth comparison between simulation ($v_{pf} = 2.9$ nm/s, $v_{pe} = 3$ nm/s, $v_{se} = 30$ nm/s, and $t_{proc} = 10$ min) and experiment (temperature $= -120$ °C, inductively coupled plasma (ICP) power $= 1000$ W, bias voltage $= -10$ V, O_2 flow $= 10$ sccm, SF_6 flow $= 200$ sccm, pressure $= 1.5$ Pa, and processing time $= 10$ min). Experimental data was obtained by FIB nanotomography; the insets show three of the FIB slices used in the analysis.

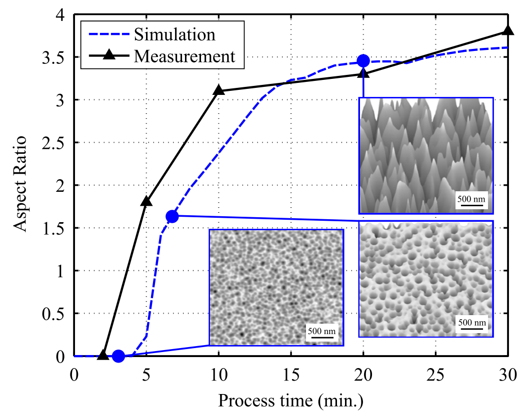

FIG. 3 (color online). Dynamic study of BSi aspect ratio evolution with time, comparing simulation ($v_{pf} = 3.1$ nm/s, $v_{pe} = 3$ nm/s, and $v_{se} = 30$ nm/s) and experimental data from [11] (Temperature $= -120$ °C, ICP power $= 1000$ W, bias voltage $= -10$ V, O_2 flow $= 10$ sccm, SF_6 flow $= 200$ sccm, and pressure $= 1.5$ Pa). The insets show the simulated BSi structure at different times through the etch process.

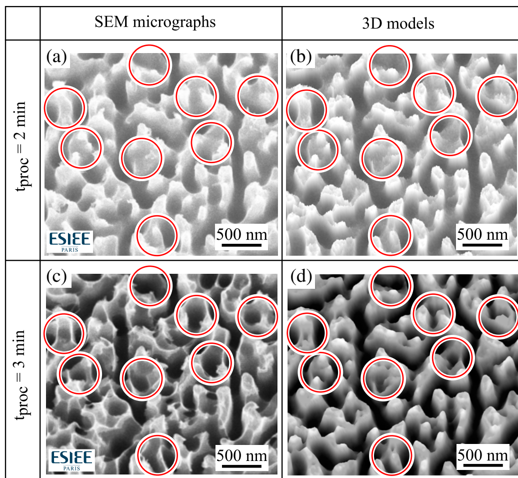

FIG. 4 (color online). Time-lapse data showing the evolution of a sample between $t = 2$ min and $t = 3$ min of process time, for both simulation and experiment. 20° tilted view of (a) initial time-lapse SEM and (b) three-dimensional reconstruction; (c) final time-lapse SEM (Temperature $= -120$°C, ICP power $= 1000$ W, bias voltage $= -10$ V, O_2 flow $= 20$ sccm, SF_6 flow $= 200$ sccm, and pressure $= 1.5$ Pa), and (d) final time-lapse simulation ($v_{pf} = 1.8$ nm/s, $v_{pe} = 1.2$ nm/s, and $v_{se} = 30$ nm/s). Preferentially etched holes at topographical saddle points are highlighted with circles.

etching conditions there are effectively shifted downwards on the phase diagram of Fig. 1, towards the uniform etching regime. Likewise, the tops of needles are overpassivated due to increased exposure to the diffusing passivating species, whereas the exposure to passivation etching species remains essentially unchanged. This pushes the effective etching condition for needle tops upwards on the phase diagram, resulting in slower (or no) etching. However, on a sample that has already developed the characteristic BSi topography, saddle points are the only areas where the effective passivation growth and etch rates are balanced, which allows the formation of new holes and explains the observed densification of the hole pattern with time.

By using a nondestructive SEM gray scale-to-height conversion (using a technique similar to [17]), we were able to construct an accurate three-dimensional model of the sample from Fig. 4(a), as can be seen by comparing with Fig. 4(b). We used this three-dimensional topography as the starting geometry for our model and performed a 1 min simulation. The resulting geometry [Fig. 4(d)] shows a remarkable resemblance to the experimental data [Fig. 4(c)], including the development of new etch fronts at topographical saddle points observed in the experimental data. This phenomenon has also been reproduced on separate simulations using mathematically generated starting surfaces (animation available as Supplemental Material [18]).

In conclusion, a combination of experimental data and modeling has allowed us to explain some of the properties of BSi, and to gain insight into the mechanisms underlying its formation by cryogenic RIE. We have shown that the observed evolution of BSi from a planar substrate can be accurately modeled by including the long-range effects of geometric occlusion (or self-shadowing). The resulting simulation model, corroborated with experimental observations, allowed us to create a phase diagram that indicates the combinations of control parameters giving rise to BSi formation and their effect on the final BSi aspect ratio. The complex geometry of BSi, consisting of needles and holes of various heights and depths, is captured by the model and explains the exceptionally low reflectivity of BSi. The dynamics of BSi formation, including the early-stage development of new etch fronts at topographical saddle points, as well as the late-stage evolution of aspect ratio with process time, are correctly predicted by the model.

The authors would like to thank Professor Tarik Bourouina for useful discussions.

[1] H. Jansen, M. de Boer, R. Legtenberg, and M. Elwenspoek, J. Micromech. Microeng. **5**, 115 (1995).

[2] T.-H. Her, R. J. Finlay, C. Wu, S. Deliwala, and E. Mazur, Appl. Phys. Lett. **73**, 1673 (1998).

[3] J. Oh, H.-C. Yuan, and H. M. Branz, Nat. Nanotechnol. **7**, 743 (2012).

[4] M. Steglich, D. Lehr, S. Ratzsch, T. Käsebier, F. Schrempel, E.-B. Kley, and A. Tünnermann, Laser Photonics Rev. **8**, L13 (2014).

[5] X. Zhang, Q. Di, F. Zhu, G. Sun, and H. Zhang, Micro & Nano Lett. **6**, 947 (2011).

[6] Y.-F. Huang *et al.*, Nat. Nanotechnol. **2**, 770 (2007).

[7] J. E. Carey, C. H. Crouch, M. Shen, and E. Mazur, Opt. Lett. **30**, 1773 (2005).

[8] V. Jokinen, L. Sainiemi, and S. Franssila, Adv. Mater. **20**, 3453 (2008).

[9] S. Wahl, F. Marty, N. Pavy, B. Mercier, and D. E. Angelescu, in *Proceedings of the IEEE International Conference on Micro Electro Mechanical Systems (MEMS), San Francisco* (IEEE, New York, 2014), p. 797.

[10] R. Dussart, X. Mellhaoui, T. Tillocher, P. Lefaucheux, M. Volatier, C. Socquet-Clerc, P. Brault, and P. Ranson, J. Phys. D **38**, 3395 (2005).

[11] K. Nguyen, P. Basset, F. Marty, Y. Leprince-Wang, and T. Bourouina, J. Appl. Phys. **113**, 194903 (2013).

[12] M. Kroll, T. Käsebier, M. Otto, R. Salzer, R. Wehrspohn, E.-B. Kley, A. Tünnermann, and T. Pertsch, in *Proceedings of the SPIE Photonics for Solar Energy Systems III, Brussels, Belgium*, edited by R. B. Wehrspohn and A. Gombert (SPIE, Bellingham, WA, 2010), p. 772505.

[13] P. Meakin, Phys. Rep. **235**, 189 (1993).

[14] J. H. Yao and H. Guo, Phys. Rev. E **47**, 1007 (1993).

[15] J. T. Drotar, Y.-P. Zhao, T.-M. Lu, and G.-C. Wang, Phys. Rev. B **62**, 2118 (2000).

[16] M. Pelliccione, T. Karabacak, and T.-M. Lu, Phys. Rev. Lett. **96**, 146105 (2006).

[17] F.-Y. Zhu, Q.-Q. Wang, X.-S. Zhang, W. Hu, X. Zhao, and H.-X. Zhang, Nanotechnology **25**, 185705 (2014).

[18] See Supplemental Material at http://link.aps.org/supplemental/10.1103/PhysRevLett.113.265502 for additional model details and simulations.